

Dynamical stability by spin transfer in nearly isotropic magnets

Received: 1 June 2025

Accepted: 21 January 2026

Published online: 04 March 2026

 Check for updates

Hidekazu Kurebayashi^{1,2,3,4,5}✉, Joseph Barker⁶, Takumi Yamazaki⁴,
Varun K. Kushwaha⁴, Kilian D. Stenning⁷, Harry Youel^{1,8}, Xueyao Hou⁴,
Troy Dion^{3,4}, Daniel Prestwood^{1,2,7}, Gerrit E. W. Bauer^{3,4,5,9},
Kei Yamamoto¹⁰✉ & Takeshi Seki^{3,4}✉

Spin transfer torques (STTs) control magnetization by electric currents, enabling a range of nano-scale spintronic applications. They can destabilize the equilibrium magnetization state by counteracting magnetic relaxation. Here we maximize the STT effect through a dedicated growth-annealing protocol for CoFeB thin films, such that magnetic anisotropies originating from the interface and shape almost cancel each other. The nearly isotropic magnets enable low-current dynamical stabilization of the magnetization in the direction opposite to an applied magnetic field, thereby realizing a spintronic analogue of the Kapitza pendulum. In an intermediate current regime, the STT drives large magnetization vector fluctuations that cover the entire Bloch sphere. The continuous variable associated with the stochastic magnetization direction may serve as a resource for probabilistic computing and neuromorphic hardware. Our results establish isotropic magnets as a platform to study as-yet-uncharted, far-from-equilibrium spin dynamics including anti-magnonics, with promising implications for unconventional computing paradigms.

A rigid pendulum whose pivot is forced to vibrate up and down, known by the name of Kapitza¹, has inspired generations of physicists^{2–4}. Under fast actuation, the bob appears to defy gravity by staying close to the upright position (Fig. 1a), demonstrating so-called dynamical stability⁵. It represents a real-world example of a controllable nonlinear dynamical system that exhibits a range of steady states in the long term, called attractors⁶, such as complex periodic orbits⁷, as well as chaotic motion⁸. The fixed distance between the bob and the pivot drastically simplifies the equation of motion but preserves the nonlinearity that causes the counter-intuitive dynamics.

Magnetic order shares the rigidity of a pendulum because the high exchange energy cost of modulating the saturation magnetization

M_s constrains the vector \mathbf{M} to the Bloch sphere with radius M_s . The Landau–Lifshitz–Gilbert (LLG) torque equation, a cousin of Newton’s second law, relates the rate of change of the spin angular momentum density $-\gamma^{-1}d\mathbf{M}/dt$ to the sum of various torques per volume $\mathbf{M} \times \delta_{\mathbf{M}}U + \boldsymbol{\tau}$ that act on the magnetization. Here $\gamma > 0$ is the modulus of the gyromagnetic ratio, U is the magnetic free energy, $\delta_{\mathbf{M}}$ denotes the functional derivative with respect to \mathbf{M} and $\boldsymbol{\tau}$ includes the viscous Gilbert damping⁹ and other torques that do not conserve U . Most studies focus on switching the magnetic order between the north and south poles of the Bloch sphere, which are the energy minima in the presence of a uniaxial anisotropy. This bistability is employed in magnetic memory applications¹⁰ in which the two poles of a small magnetic medium

¹London Centre for Nanotechnology, University College London, London, UK. ²Department of Electronic and Electrical Engineering, University College London, London, UK. ³Center for Science and Innovation in Spintronics, Tohoku University, Sendai, Japan. ⁴Institute for Materials Research, Tohoku University, Sendai, Japan. ⁵WPI Advanced Institute for Materials Research, Tohoku University, Sendai, Japan. ⁶School of Physics and Astronomy, University of Leeds, Leeds, UK. ⁷Blackett Laboratory, Imperial College London, London, UK. ⁸Department of Physics and Astronomy, University College London, London, UK. ⁹Kavli Institute for Theoretical Sciences, University of the Chinese Academy of Sciences, Beijing, China. ¹⁰Advanced Science Research Center, Japan Atomic Energy Agency, Tokai, Japan. ✉ e-mail: h.kurebayashi@ucl.ac.uk; yamamoto.kei@jaea.go.jp; takeshi.seki@tohoku.ac.jp

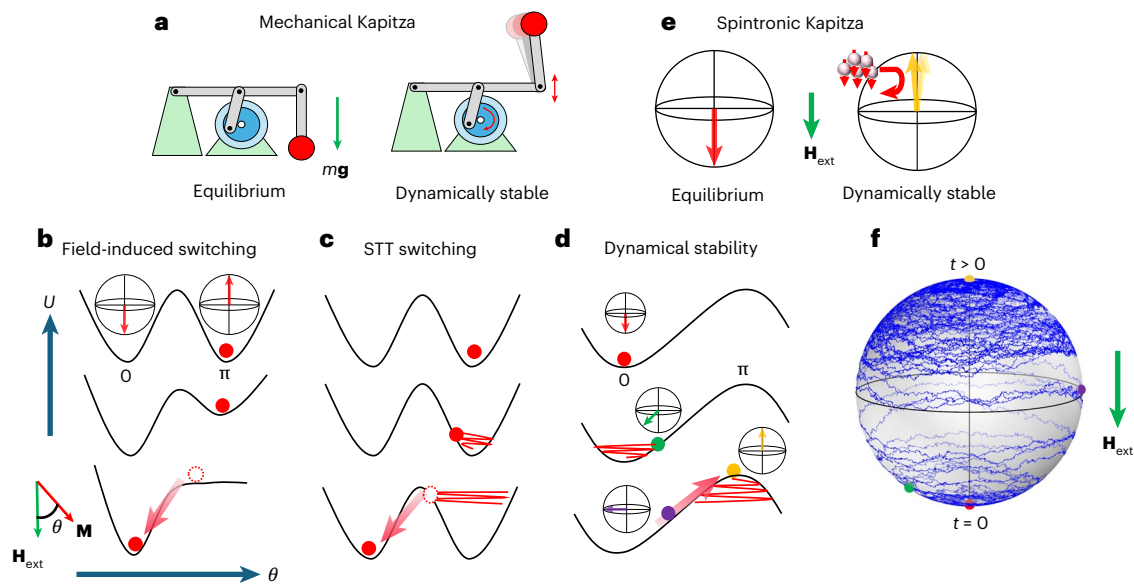


Fig. 1 | Dynamical stability of the spintronic Kapitza pendulum. **a**, Schematics of the mechanical Kapitza pendulum with and without an external drive. mg represents the gravitational force on the bob. **b–d**, Schematics of different magnetization switching and stability processes illustrated within the angular dependence of magnetic energy (U): field-induced switching (**b**), STT switching (**c**) and dynamical stability (**d**). θ is defined by the relative angle between the external magnetic field (H_{ext}) and magnetic moment (M). See below for the mechanism of each process. **e**, Analogy between the Kapitza pendulum and dynamical stabilization by spin transfer in an isotropic magnet. The magnetic field provides

a minimum and maximum of potential energy as the gravitational field does, and the STT plays the role of dynamical driving that controls their stability. Note that the arrows piercing through the conduction electrons (solid spheres) represent their spin pointing opposite to their magnetic moment. **f**, A typical solution of the stochastic LLG equation for a macrospin in an isotropic magnet. The initial condition is set at the south pole (red dot) and due to the anti-damping STT exceeding the Gilbert damping torque, the state precesses away from the field direction and settles around the inverted state (yellow dot). The coloured dots on the sphere have the corresponding potential energy values indicated in **d**.

represent a single bit that can be read out electrically by the celebrated giant/tunnelling magnetoresistance (MR)^{11–14}. The barrier between the energy minima is sufficiently higher than the thermal energy to retain the information safely^{15–17}.

A static magnetic field tilts the free energy double-well and favours one of the two minima into which the magnetization settles in equilibrium (Fig. 1b). The magnetization can be flipped by reversing the magnetic field but also electrically using current-induced spin transfer from spin-polarized conduction electrons^{18,19} that contributes to τ without affecting U (ref. 20). This effect, so-called spin transfer torques (STTs)^{21–23}, may counteract the magnetic dissipation that stabilizes the magnetization against fluctuations around a free energy minimum²⁴. When it overcomes the damping, the equilibrium becomes unstable, sending the system into motion, similar to what the oscillating pivot does to a rigid pendulum. In the presence of a large magnetic anisotropy, the switching is between the potential minima and non-volatile^{25–27} as illustrated in Fig. 1c. Two decades ago, a volatile current-driven switching behaviour was observed once the applied magnetic field exceeds the anisotropy field²⁸. It was subsequently identified to be a dynamical stabilization at a potential maximum^{29–31} (Fig. 1d), reminiscent of the Kapitza pendulum. The physical mechanism is different, however, in the dissipative nature of STT contrasted to the effective conservative potential description of the driven pendulum where the inverted state is a local minimum¹. The high field and current density required for the dynamical stability in the hard magnetic layers in a nanopillar structure hindered further investigation of this regime.

In this study, we employ magnetic films with vanishingly small magnetic anisotropy as a material platform to investigate dynamical stability and associated nonlinear phenomena. As a model system, we use prototypical MgO|CoFeB|W multilayers in which the demagnetizing field in the thin-film magnets favours CoFeB magnetization within the film plane but can be counter-balanced by an interface-induced perpendicular magnetic anisotropy^{15–17} (PMA) controlled by

post-growth annealing (see Supplementary Note 1 for more details). We drive its nonlinear dynamics by the STT generated by the spin-orbit interaction in the tungsten layer (spin-orbit torque, SOT)^{32–34}. Two independent electrical measurements confirm that the STT forces the magnetization into a steady state residing at the free energy maximum, contradicting the common wisdom that the attractor state under a large STT is an auto-oscillation, a particular kind of nonlinear periodic orbit that appears as uniform and localized spin-wave modes^{35–40}. A vanishing anisotropy suppresses auto-oscillations and drastically reduces the critical current to drive the magnet into the nonlinear dynamical regime. Our analytical estimates and numerical simulations (for example, Fig. 1f) show that the probability distribution of the magnetization direction on the sphere can be controlled at will by the current and field. This whole Bloch sphere sampling might resource a continuous variable for probabilistic computation hardware, different from currently studied binary magnetic systems^{41,42}. Our devices serve as a foundation for studying nonlinear dynamics of a complex many-body system that can be understood by a simple model.

Minimizing the magnetic anisotropy

We grew multilayer stacks of MgO(3 nm)|CoFeB(2 nm)|W(3 nm) in an ultrahigh vacuum sputtering system on thermally oxidized Si at room temperature (Methods). As-grown films are easy-plane magnets due to strong demagnetizing fields of magnitude M_s . The PMA from the CoFeB|MgO interface^{43,44} tends to pull the magnetization out of plane which can be incorporated by an effective magnetization $M_{\text{eff}} = M_s - 2K_{\perp}/(\mu_0 M_s)$, where K_{\perp} is the perpendicular interface anisotropy constant and μ_0 is the permeability of vacuum. By careful growth and post-annealing we tune the system to $M_{\text{eff}} \approx 0$ as explained in Supplementary Note 1.

In the coordinate system in the inset of Fig. 2a, the spin-Hall effect initiates the spin transfer by converting a charge current in the x direction into a spin current normal to the interface and polarized along

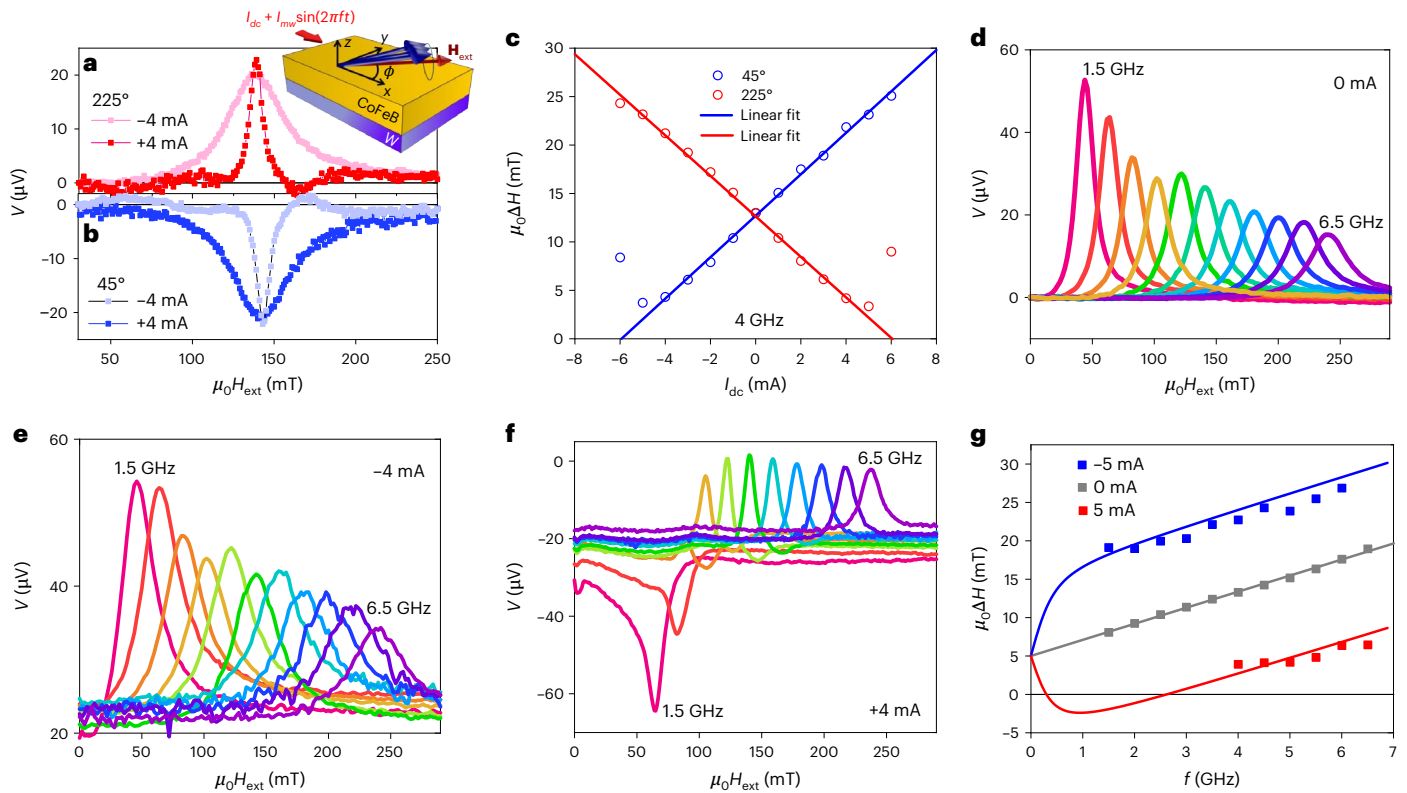


Fig. 2 | Current-induced magnetic damping probed by FMR. **a, b**, Field-swept FMR voltages measured for $\phi = 225^\circ$ (**a**) and $\phi = 45^\circ$ (**b**). The inset is a sketch of our device and the coordinate system. **c**, Linewidth extracted from FMR at 4 GHz with $\phi = 45^\circ$ (blue) and $\phi = 225^\circ$ (red), for different I_{dc} . The solid lines show the results of a linear fitting excluding points below -4 mA for 45° and above 4 mA for 225° . **d–f**, Field-swept FMR voltages measured for various frequencies (0.5 GHz

separations) and three values of I_{dc} at 0 mA (**d**), -4 mA (**e**) and 4 mA (**f**). Magnetic fields were applied along $\phi = 225^\circ$. **g**, Linewidth as a function of frequency for different I_{dc} , that is $+5$, 0 and -5 mA, represented by the red, grey and blue dot, respectively. The measurements were carried out at $\phi = 225^\circ$. The grey line is a linear fitting of the 0 mA data. Both red and blue curves are calculated using equation (2).

the y direction^{32,45}. The SOT arising from a d.c. current I_{dc} destabilizes the equilibrium $\mathbf{M} \parallel \mathbf{H}_{ext}$ at a critical value I_c (refs. 28,29,46) that solves

$$-\beta I_c \sin \phi = \alpha \left(H_{ext} + \frac{M_{eff}}{2} \right) + \Delta H'_0, \quad (1)$$

where α , H_{ext} and ϕ are the Gilbert damping constant, the external magnetic field magnitude and the angle between the x axis and \mathbf{H}_{ext} applied within the film plane, respectively. β is a phenomenological parameter proportional to the spin-Hall angle θ_{SH} (Methods) that characterizes the efficiency of the charge-to-spin conversion. In Supplementary Note 3, we explain that the current-induced self-torque in the CoFeB layer is negligibly small because electrons flow primarily in the W layer. Spatial variations of the material parameters require the introduction of a constant offset $\Delta H'_0$. We can reduce the critical current by minimizing M_{eff} , as expected.

Current rectification in the inverted state

The dynamical stability of the anti-parallel state $\mathbf{M} = (M_x, M_y, M_z)^T \parallel -\mathbf{H}_{ext}$ at large negative currents I_{dc} can be detected by measuring the spin-Hall MR (SMR)^{47,48} in static and dynamical regimes. The angular dependence of the electric resistance reads $R = R_0 + \Delta R_{SMR}(1 - M_y^2/M_s^2)$ (ref. 47). See detailed experiments of SMR in Supplementary Note 3. Here R_0 is the bulk resistance, whereas ΔR_{SMR} can be calculated by spin-diffusion theory with appropriate boundary conditions⁴⁸ and/or fitted to the experiments. When a microwave current $I_{mw} \cos(2\pi ft)$ at frequency f modulates I_{dc} , the induced ac SOT causes a small oscillation $M_s \delta m_y$ in M_y , that, in turn, affects the electric resistance. The resulting rectified voltage V as a

function of f and H_{ext} is monitored by the spin-torque ferromagnetic resonance (ST-FMR)^{45,49,50}. According to Supplementary Note 4, the resonance field and current-dependent linewidth are given by

$$H_{res}^\pm = \sqrt{4\pi^2 f^2 / (\gamma \mu_0)^2 + M_{eff}^2} / 4 \mp M_{eff} / 2 \text{ and}$$

$$\Delta H_\pm = \Delta H_0 \pm \frac{2\pi f}{\gamma \mu_0} \left(\alpha + \frac{\beta I_{dc} \sin \phi}{H_{res}^\pm \pm M_{eff} / 2} \right), \quad (2)$$

respectively, where the upper (lower) sign holds for the parallel (anti-parallel) state, and an inhomogeneous broadening ΔH_0 is assumed independent of the magnetization direction. To the leading order, $V \approx -2\Delta R_{SMR} I_{mw} (M_y / M_s) \delta m_y \cos(2\pi ft)$, where the overbar denotes time averaging over a period. As $\delta m_y \approx \beta I_{mw} \cos(2\pi ft) / \Delta H_\pm$ at $H_{ext} = H_{res}^\pm$ and $\Delta H_\pm > 0$ whenever $\mathbf{M} \parallel \pm \mathbf{H}_{ext}$ is stable, V changes sign on magnetization reversal. With $M_y = \pm M_s \sin \phi$, the H_{ext} dependence of V is given by

$$V = \mp \Delta R_{SMR} \beta I_{mw}^2 \frac{2\pi f / (\gamma \mu_0)}{2H_{res}^\pm \pm M_{eff}} \frac{\Delta H_\pm \cos^2 \phi \sin \phi}{(H_{ext} - H_{res}^\pm)^2 + \Delta H_\pm^2}. \quad (3)$$

The Lorentzian approximation (equation (3)) breaks down when $H_{ext} \approx H_{res}^\pm$ and $\Delta H_\pm \approx 0$ simultaneously (Supplementary Note 4).

Dynamical stability

Figure 2 summarizes our ST-FMR experiments on devices fabricated from magnetic multilayers with vanishing anisotropies as shown in Supplementary Fig. 1f. The ferromagnetic resonance (FMR) traces for $\phi = 45^\circ$ and 225° under applied currents $I_{dc} = \pm 4$ mA at $f = 4$ GHz in Fig. 2a,b display clear linewidth changes⁵¹ as predicted by equation (2).

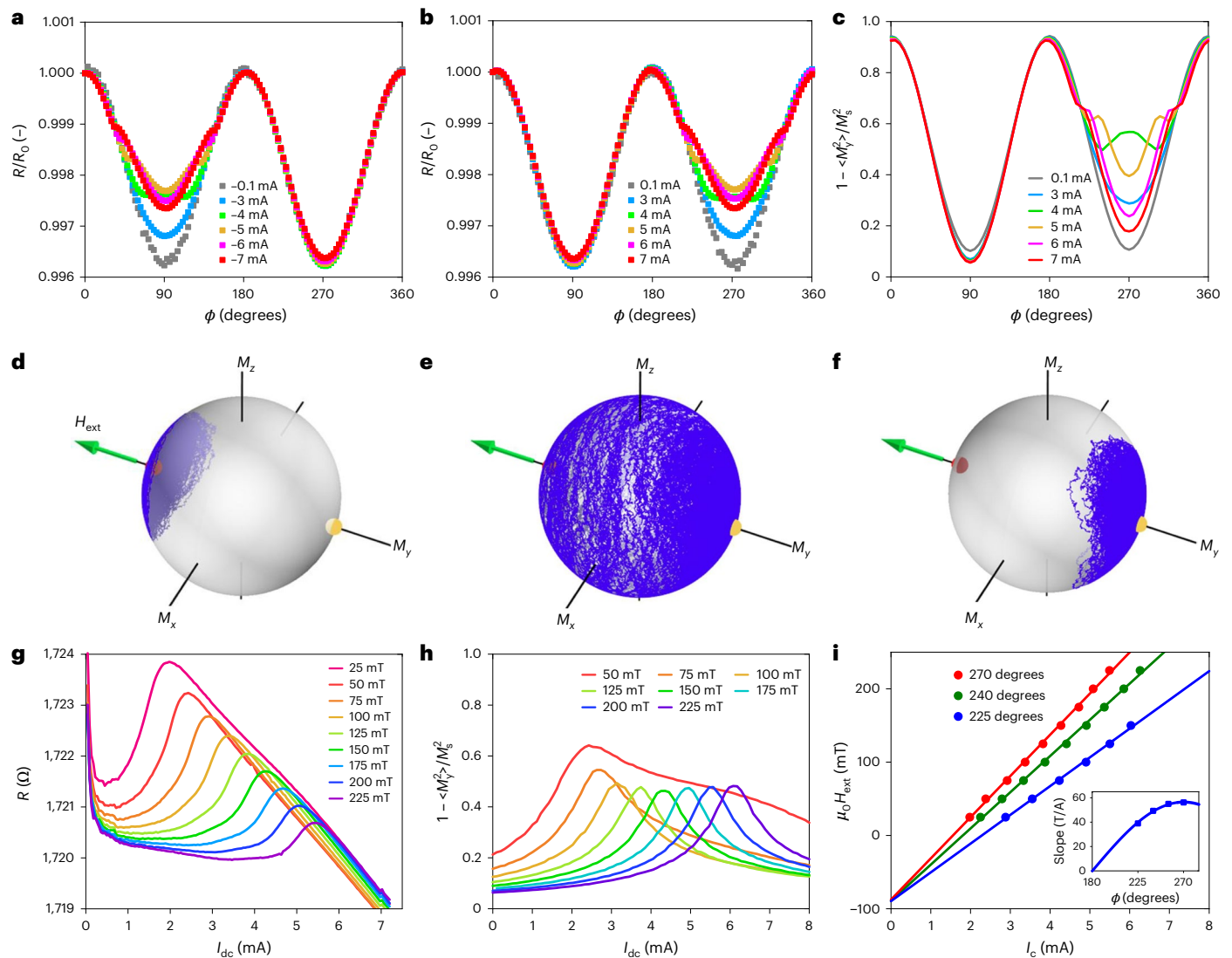


Fig. 3 | Electric resistance probes for magnetic fluctuations and the inverted states. **a, b**, Observed angular MR in the coordinate system of Fig. 2a for negative (a) and positive (b) currents, normalized by the resistance at $\phi = 0^\circ$ for each current. **c**, $1 - \langle M_y^2 \rangle / M_s^2$ calculated by the stochastic LLG equation in the macrospin approximation. **d–f**, Time-dependent trajectories of the macrospin moment calculated by the stochastic LLG equation for currents 0.1 mA (d), 4.1 mA (e) and 7 mA (f) and $\phi = 270^\circ$. The field strength is 125 mT for **a–f**. **g**, Resistance versus d.c. current measurements for applied magnetic fields 25–200 mT along $\phi = 270^\circ$. **h**, Calculated $1 - \langle M_y^2 \rangle / M_s^2$ as a function of current and applied magnetic field. **i**, I_c extracted in **g** for different field strengths and angles (dots) and linear fits (lines). The inset shows the slope (dots) and a fit by $\sin \phi$ (curve).

The resonance fields H_{res} and linewidths ΔH extracted by a double Lorentzian fit (Methods) are plotted in Fig. 2c and confirm the linear relationship between ΔH and I_{dc} up to currents close to I_c defined by equation (1). At higher currents, the system becomes increasingly unstable, and ΔH increases again. Linear extrapolation to zero ΔH gives $I_c \approx 6$ mA at $\mu_0 H_{ext} = \mu_0 H_{res} \approx 140$ mT or a current density of 2×10^{11} A m⁻², which is approximately one order of magnitude smaller than the typical values for the onset of auto-oscillation in anisotropic magnets^{37,52}, due to the minimized M_{eff} . The deviation from the linear relation near I_c reflects the aforementioned breakdown of equation (3).

The FMR lineshape for $\phi = 225^\circ$ and I_{dc} of 0 and -4 mA in Fig. 2d,e affirms the expected modulation of ΔH , whereas fitting the field-frequency relation of the peak frequencies by the Kittel formula yields the residual easy-plane anisotropy of $\mu_0 M_{eff} = 37.3$ mT, which is indeed much smaller than $\mu_0 M_s$ of CoFeB (-1.5 T)⁵³. At $I_{dc} = 4$ mA in Fig. 2f, V changes its sign at low frequencies, which is strong evidence of the dynamical stabilization of the anti-parallel state $\mathbf{M} \parallel -\mathbf{H}_{ext}$ for $\mu_0 H_{ext} \lesssim 100$ mT. This also agrees with equation (1) where $I_c = 4$ mA for $\phi = 225^\circ$ and $\mu_0 H_{ext} = 100$ mT. The fit of the linear relation in Fig. 2c leads to

$\theta_{SH} = 0.22$, which is similar to published values⁵⁴ and $\beta = 2.6 \times 10^6$ m⁻¹. We confirm the sign reversal of the ST-FMR peaks for small f and H_{ext} in different samples as shown in Supplementary Fig. 10. Equation (2) offers a quantitative test of our interpretation. For $2\pi f / \gamma \gg |M_{eff}|$ and $H_{res}^+ + M_{eff} / 2 \propto f$, ΔH becomes a linear function of f with a slope $2\pi\alpha / \gamma\mu_0$ that does not depend on I_{dc} . Figure 2g verifies this prediction, as I_{dc} mainly produces the ΔH offset of $2\pi f \beta I_{dc} \sin \phi / \sqrt{4\pi^2 f^2 + \gamma^2 \mu_0^2 M_{eff}^2} / 4$ for $2\pi f \gg \gamma \mu_0 M_{eff}$, in agreement with the curves that represent equation (2) for the upper signs with $\alpha = 0.053$ and $\mu_0 \Delta H_0 = 5$ mT.

Electric resistance probes magnetic fluctuations

The thermal fluctuations of the magnetization angle affect its time-averaged properties. In particular, when the stability of both poles near the critical current weakens, the magnetization becomes susceptible to even small random torques. Because the time scales associated with the motion of conduction electrons (femtosecond) are much faster than those of magnetic fluctuations (nanosecond), the SMR probes the expectation value of M_y^2 , that is, $R = R_0 + \Delta R_{SMR} (1 - \langle M_y^2 \rangle / M_s^2)$, in which the angled brackets denote temporal and spatial averaging⁴⁷.

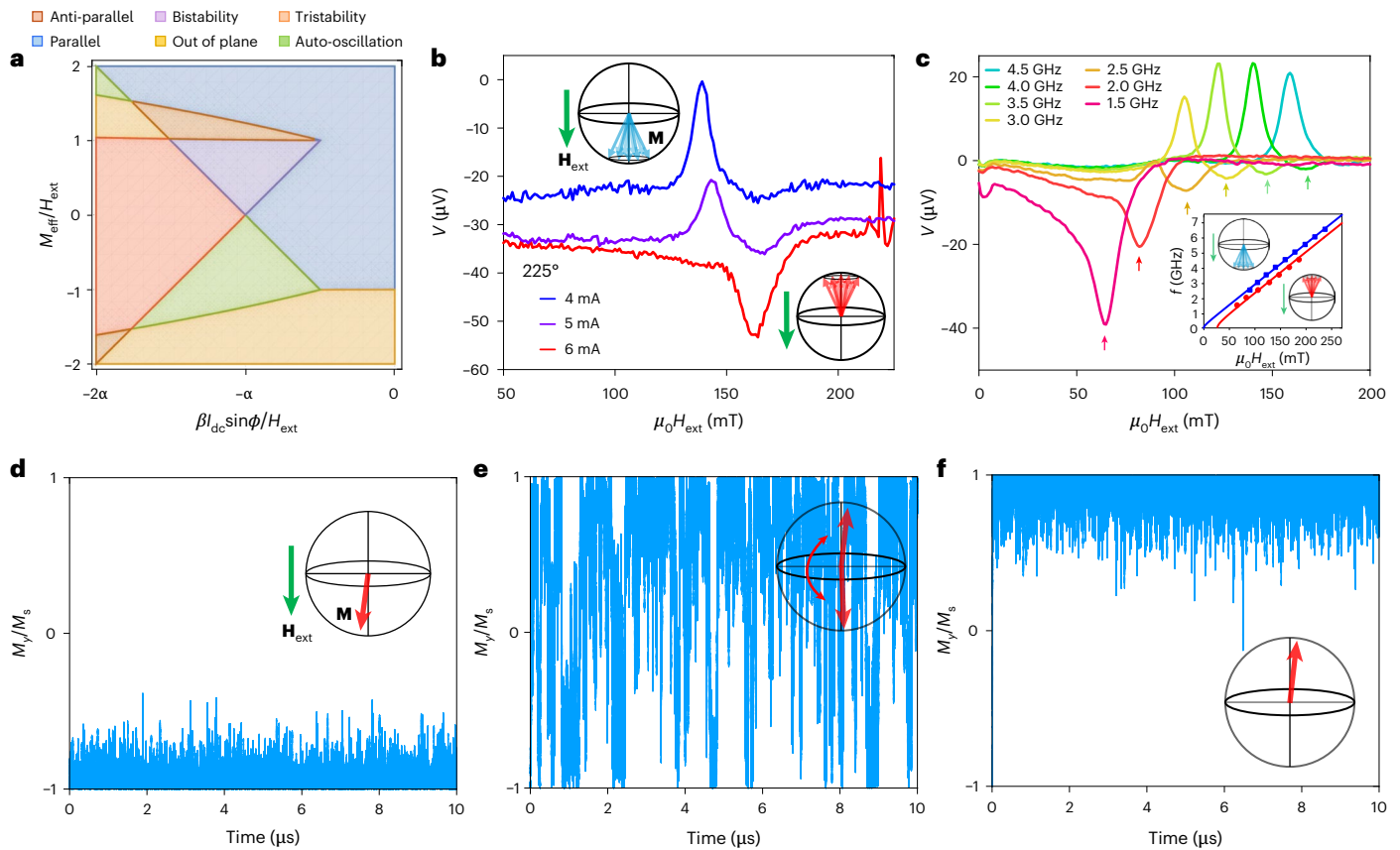


Fig. 4 | Stability diagram, bistability and probabilistic distribution for nearly isotropic magnets. **a**, Bifurcation diagram constructed from the stationary solutions of the LLG equation. **b**, ST-FMR for different I_{dc} close to the damping compensation condition. When a larger I_{dc} increases the anti-damping torques beyond the critical value, the magnetization precesses around the dynamically stable state at the north pole, generating an opposite d.c. voltage at resonance.

c, The ST-FMR results highlight the current-induced magnetization reversal. The inset shows the FMR frequencies as functions of field for the two magnetization directions. **d–f**, Time-dependent traces of the normalized M_y component for small (**d**)/medium (**e**)/large (**f**) anti-damping torques. Here, $M_y = -1$ is along the magnetic field direction.

Larger fluctuations of \mathbf{M} imply smaller $\langle M_y^2 \rangle$ and a higher resistance in the parallel state (see Supplementary Note 3 for more discussions in relation to unidirectional SMR^{55,56}).

Figure 3a,b shows the ϕ dependence of the MR for $\mu_0 H_{ext} = 150$ mT and different I_{dc} . Without fluctuations, $R/R_0 = 1 + (\Delta R_{SMR}/R_0)(1 - \sin^2 \phi)$, which agrees well for small applied currents $I_{dc} = \pm 0.1$ mA. Joule heating cannot explain the asymmetric distortion of the MR around $\phi = 180^\circ$ at larger $|I_{dc}|$. A strong current dependence occurs only when the field direction and spin polarization are parallel, that is, when the STT destabilizes the equilibrium magnetization. Beyond currents of 4 and 5 mA, the fluctuations appear to decrease again.

We model the magnetization fluctuations by a stochastic LLG equation that includes the thermal noise in the effective magnetic field ξ that obeys the fluctuation–dissipation relation $\langle \xi_i(t) \xi_j(t') \rangle = \delta_{ij} \delta(t - t') (2\alpha k_B T) / (\gamma(1 + \alpha^2) M_s V_a)$, where k_B is the Boltzmann constant and $V_a = 1 \times 25 \times 25$ nm³ is a magnetic coherence volume⁵⁷. The calculated $1 - \langle M_y^2 \rangle / M_s^2$ as a function of ϕ for fixed I_{dc} in Fig. 3c reproduces the salient trends observed in Fig. 3b. $\mathbf{M}(t)$ for current values $I_{dc} = 0.1, 4.1$ and 7 mA and $\phi = 270^\circ$ in Fig. 3d–f illustrate the build-up of the steady state probability distributions in Fig. 3c. For very small and large currents, at least at one of the poles the torques damp rather than amplify the thermal agitation. Close to the critical current (Fig. 3e), the magnetization vector explores the entire Bloch sphere with nearly constant probability density.

Equation (1) should hold near the resistance maxima in Fig. 3g that shift towards higher I_{dc} for larger H_{ext} but disappear when switching the field direction as shown in Supplementary Fig. 12a. At $\mu_0 H_{ext} = 150$ mT

the resistance peak height relative to lower I_{dc} is about 1–2 Ω or 0.1%, consistent with Fig. 3b at $\phi = 270^\circ$. The peaks in the calculated $1 - \langle M_y^2 \rangle / M_s^2$ in Fig. 3h correspond to a minimum in $\langle M_y^2 \rangle / M_s^2$ or maximum of the magnetic fluctuations at I_c . The differences between theory and experiments (Fig. 3g,h) are partially caused by the incomplete theoretical account of heating effects, as well as the limitation of the macrospin model to describe spatial fluctuations in our extended film geometry. Equation (1) predicts a linear relationship between H_{ext} and I_c with a negative intercept. Figure 3i illustrates the linear field-current relationship observed at the resistance maximum. A fit to the ϕ dependence of the slope (Fig. 3i, inset, and Supplementary Fig. 11e) leads to the ratio $\theta_{SH}/\alpha = 3.7$. Substituting $\alpha = 0.053$ from the ST-FMR, $\theta_{SH} = 0.20$ agrees well with $\theta_{SH} = 0.22$ found above from an independent experiment on the same sample. Using equation (1) with the experimental parameters α and M_{eff} and the zero-current intercept in Fig. 3i, $\mu_0 \Delta H'_0 = 3.8$ mT, comparable to the inhomogeneous broadening $\mu_0 \Delta H_0 = 5.0$ mT as deduced from the ST-FMR.

Stochastic switching in nearly isotropic magnets

Both ST-FMR and MR measurements find a residual easy-plane anisotropy $M_{eff} > 0$ that, albeit small, causes an effect on the nonlinear dynamics that deserves a more detailed study. Figure 4a shows a bifurcation (or dynamical phase) diagram that analytically classifies the asymptotic final states of the deterministic LLG equation as a function of dimensionless parameters $\beta I_{dc} \sin \phi / H_{ext}$ and M_{eff} / H_{ext} (see Supplementary Note 5 for more details). Since the Poincaré–Bendixon theorem⁵⁸ excludes chaos on a sphere, the attractors in the absence of stable

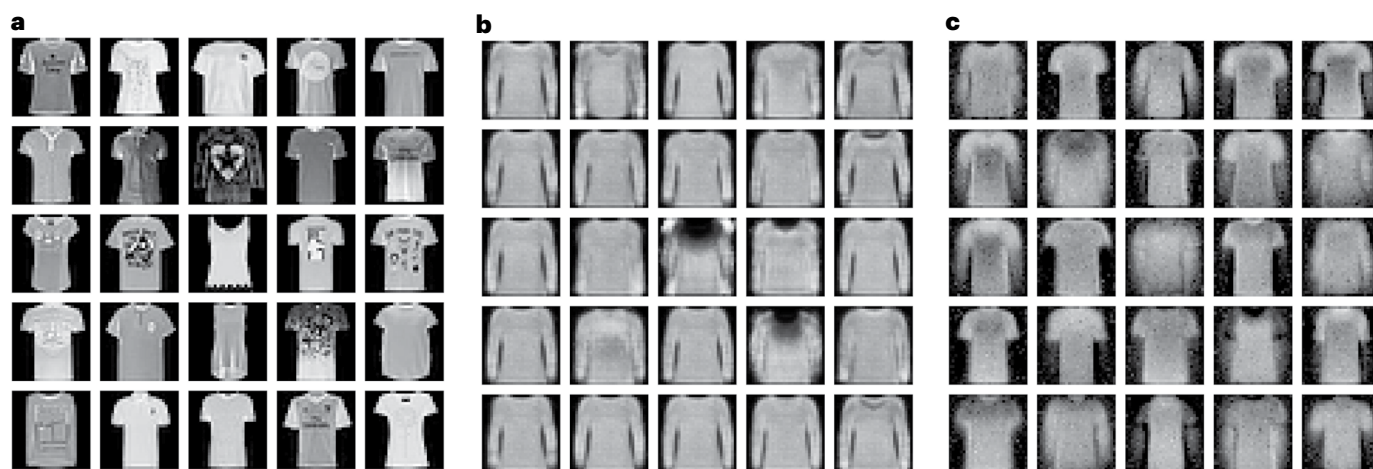


Fig. 5 | Two-dimensional image generation by a continuous RBM with electrically controlled zero-damping states in isotropic magnets. **a**, Samples of the Fashion-MNIST training data (t-shirt class). **b,c**, Generated data using binary and continuous variables for the visible nodes, respectively.

time-independent solutions must be finite-angle precessional states. The ‘auto-oscillations’ that occupy the regions shaded in green exist for $M_{\text{eff}} > 0$ only when the anisotropy and STT are very large. We identify a regime around the damping compensation $-\beta I_{\text{dc}} \sin \phi / H_{\text{ext}} = \alpha$, in which the inverted state is dynamically stabilized by a current that is smaller than the estimate by equation (1) for $M_{\text{eff}} = 0$. We may explain this deviation in terms of a dynamical bistability, also observed in the simulations in Fig. 3e in the form of a bimodal probability density at the critical current.

The experiments show clear signatures of this bistability. The ST-FMR voltages in Fig. 4b change sign with increasing I_{dc} . The FMR mode around $\mathbf{M} \parallel \mathbf{H}_{\text{ext}}$ at $\mu_0 H_{\text{ext}} \approx 140$ mT gradually disappears, and an inverted peak emerges at a higher field $\mu_0 H_{\text{ext}} \approx 160$ mT. This observation supports the prediction of different resonance fields $H_{\text{res}}^+ - H_{\text{res}}^- = -M_{\text{eff}}$ in equation (3). At $I_{\text{dc}} = 5$ mA, two peaks are observed. The one at $\mu_0 H_{\text{ext}} \approx 140$ mT for $\mathbf{M} \parallel \mathbf{H}_{\text{ext}}$ is, according to equation (1), stable at higher fields. The inverted peak at $\mu_0 H_{\text{ext}} \approx 160 > 140$ mT, indicates the need for two independent stability criteria. Figure 4c also shows two peaks in ST-FMR voltages at different frequencies and a fixed current of $I_{\text{dc}} = 4$ mA for $100 \text{ mT} \lesssim \mu_0 H_{\text{ext}} \lesssim 170$ mT. Theory predicts different resonance conditions for the parallel and inverted states $2\pi f_{\text{res}}^{\pm} = \gamma \mu_0 \sqrt{H_{\text{ext}} (H_{\text{ext}} \mp M_{\text{eff}})}$ for $\mathbf{M} \parallel \pm \mathbf{H}_{\text{ext}}$ respectively, consistent with H_{res} in the inset of Fig. 4c, which allows us to estimate $\mu_0 M_{\text{eff}} \approx 30 \pm 5$ mT.

Our discovery of dynamically stabilized states opens a vast and unexplored field of research. The numerical solutions of the stochastic LLG equation for $M_{\text{eff}}/H_{\text{ext}} = 0.31$ in Fig. 4d–f show drastic changes of the probabilistic distribution when relaxing the constraint of a strong anisotropy. At an intermediate current $I_{\text{dc}} = 4.0$ mA, the magnetization visits all angles of the Bloch sphere with comparable probability. The characteristic dwell time around the poles in Fig. 4e is in the submicrosecond range, consistent with a semi-analytical estimate from the ‘first-passage time’ theory^{59,60} (Supplementary Note 7). It is predicted to be highly tunable through an exponential dependence on a Boltzmann factor $\mu_0 M_s H_{\text{ext}} V_a / k_B T$, which can be probed by time-resolved optical or electric measurements. An analytical solution of the Fokker–Planck equation corresponding to the stochastic LLG for $M_{\text{eff}} = 0$ gives the same exponential dependence on $\mu_0 M_s H_{\text{ext}} V_a / k_B T$ of the MR versus I_{dc} (Supplementary Note 6). Supplementary Fig. 12, on the other hand, shows that the current dependence of the MR is remarkably robust across a wide range of temperature. We attribute the discrepancies to spatial fluctuations in the film beyond the macrospin model, such as sample inhomogeneities, domain formation or spin-wave instabilities of the anti-parallel state⁶¹. Furthermore, our understanding

of the crystalline, compositional and thickness inhomogeneities and their effects on the critical currents is incomplete, as is our interpretation of $\Delta H'_0$ in equation (1).

Electrically controlled zero-damping states in isotropic magnets provide a computational resource that samples continuous random variables from the entire Bloch sphere, physically modelling a continuous restricted Boltzmann machine^{62,63} (RBM). We use this model to generate two-dimensional images via an unsupervised machine learning framework. In this scheme, we define visible and hidden layers connected by trainable weights and apply individual biases on each node (see Supplementary Note 9 for more details). The continuous nodes in the visible layer are represented by the magnetization dynamics of an STT-driven isotropic magnet. We trained the continuous RBM and a traditional binary RBM using the Fashion-MNIST benchmark images (Fig. 5a) and at inference, generated new samples, as shown in Fig. 5b,c. The generative artificial intelligence architecture using the continuous variable outperforms those using binary variables by producing more meaningful and diverse images, which we quantitatively demonstrate using standard metrics as detailed in Supplementary Note 9. This improvement arises because, unlike the traditional RBM which is limited to generating binary image data and necessitates averaging during post processing (rate-coded RBM)^{64,65}, the continuous RBM directly generates raw image data, enabling smoother convergence and more diverse image generation. Our findings highlight the potential of these magnetic states for various computing applications, superseding conventional binary systems such as stochastic magnetic tunnel junctions acting as probabilistic bits⁶⁶.

Nearly isotropic MgO|CoFeB|W multilayers allow a dynamical stabilization of the magnetic order at the maximum of the free energy simply by applying an electric current, creating a research frontier for nonlinear and strongly out-of-equilibrium magnetic properties. Building on our time-averaged measurements on macroscopic samples that reveal the essential physics of this phenomenon, spatially and temporally resolved experiments can test phenomenological, statistical and ultimately quantum-mechanical models. In this regard, microfocus Brillouin light scattering spectroscopy would be a powerful tool²⁴. The dynamical stabilization of magnetic order has not yet played a major role in studies of magnonic and spintronic effects^{67–69}. However, the option of creating magnetic devices based on isotropic magnets that operate in inverted and dynamically bistable regimes at relatively low power levels provides radically different functionalities that may be useful for, for example probabilistic computation hardware⁷⁰. A robust dynamically stabilized state in the extended film geometry can also lead to experimental studies of recent theoretically predicted

antiparticle-like (or anti-magnonic) properties of spin waves around the reversed magnetization state⁶¹.

Note added in proof: Prior to the acceptance of our manuscript, we became aware of a preprint reporting similar results⁷¹.

Online content

Any methods, additional references, Nature Portfolio reporting summaries, source data, extended data, supplementary information, acknowledgements, peer review information; details of author contributions and competing interests; and statements of data and code availability are available at <https://doi.org/10.1038/s41563-026-02510-z>.

References

- Kapitza, P. L. Dynamic stability of a pendulum when its point of suspension vibrates. *Sov. Phys. JETP* **21**, 588–592 (1951).
- Acheson, D. J. & Mullin, T. Upside-down pendulums. *Nature* **366**, 215–216 (1993).
- Citro, R. et al. Dynamical stability of a many-body Kapitza pendulum. *Ann. Phys.* **360**, 694–710 (2015).
- Apffel, B., Novkoski, F., Eddi, A. & Fort, E. Floating under a levitating liquid. *Nature* **585**, 48–52 (2020).
- Stephenson, A. On a new type of dynamical stability. *Mem. Proc. Manch. Lit. Philos. Soc.* **52**, 1–10 (1908).
- Kuznetsov, Y. A. *Elements of Applied Bifurcation Theory* Vol. 112 (Springer, 1998).
- Acheson, D. J. Multiple-nodding oscillations of a driven inverted pendulum. *Proc. R Soc. A* **448**, 89–95 (1995).
- Blackburn, J. A. & Baker, G. L. A comparison of commercial chaotic pendulums. *Am. J. Phys.* **66**, 821–830 (1998).
- Gilbert, T. Classics in magnetics a phenomenological theory of damping in ferromagnetic materials. *IEEE Trans. Magn.* **40**, 3443–3449 (2004).
- Bhatti, S. et al. Spintronics based random access memory: a review. *Mater. Today* **20**, 530–548 (2017).
- Binasch, G., Grünberg, P., Saurenbach, F. & Zinn, W. Enhanced magnetoresistance in layered magnetic structures with antiferromagnetic interlayer exchange. *Phys. Rev. B* **39**, 4828–4830 (1989).
- Baibich, M. N. et al. Giant magnetoresistance of (001)Fe/(001)Cr magnetic superlattices. *Phys. Rev. Lett.* **61**, 2472–2475 (1988).
- Yuasa, S., Nagahama, T., Fukushima, A., Suzuki, Y. & Ando, K. Giant room-temperature magnetoresistance in single-crystal Fe/MgO/Fe magnetic tunnel junctions. *Nat. Mater.* **3**, 868–871 (2004).
- Parkin, S. S. P. et al. Giant tunnelling magnetoresistance at room temperature with MgO (100) tunnel barriers. *Nat. Mater.* **3**, 862–867 (2004).
- Ikeda, S. et al. A perpendicular-anisotropy CoFeB–MgO magnetic tunnel junction. *Nat. Mater.* **9**, 721–724 (2010).
- Yang, H. X. et al. First-principles investigation of the very large perpendicular magnetic anisotropy at Fe|MgO and Co|MgO interfaces. *Phys. Rev. B* **84**, 054401 (2011).
- Yakata, S. et al. Influence of perpendicular magnetic anisotropy on spin-transfer switching current in CoFeB/MgO/CoFeB magnetic tunnel junctions. *J. Appl. Phys.* **105**, 07D131 (2009).
- Slonczewski, J. Current-driven excitation of magnetic multilayers. *J. Magn. Magn. Mater.* **159**, L1–L7 (1996).
- Berger, L. Emission of spin waves by a magnetic multilayer traversed by a current. *Phys. Rev. B* **54**, 9353–9358 (1996).
- Tserkovnyak, Y., Brataas, A., Bauer, G. E. W. & Halperin, B. I. Nonlocal magnetization dynamics in ferromagnetic heterostructures. *Rev. Mod. Phys.* **77**, 1375–1421 (2005).
- Ralph, D. & Stiles, M. Spin transfer torques. *J. Magn. Magn. Mater.* **320**, 1190–1216 (2008).
- Apalkov, D., Dieny, B. & Slaughter, J. M. Magnetoresistive random access memory. *Proc. IEEE* **104**, 1796–1830 (2016).
- Hirohata, A. et al. Review on spintronics: principles and device applications. *J. Magn. Magn. Mater.* **509**, 166711 (2020).
- Demidov, V. E. et al. Control of magnetic fluctuations by spin current. *Phys. Rev. Lett.* **107**, 107204 (2011).
- Myers, E. B., Ralph, D. C., Katine, J. A., Louie, R. N. & Buhrman, R. A. Current-induced switching of domains in magnetic multilayer devices. *Science* **285**, 867–870 (1999).
- Mangin, S. et al. Current-induced magnetization reversal in nanopillars with perpendicular anisotropy. *Nat. Mater.* **5**, 210–215 (2006).
- Liu, L. et al. Spin-torque switching with the giant spin hall effect of tantalum. *Science* **336**, 555–558 (2012).
- Katine, J. A., Albert, F. J., Buhrman, R. A., Myers, E. B. & Ralph, D. C. Current-driven magnetization reversal and spin-wave excitations in Co/Cu/Co pillars. *Phys. Rev. Lett.* **84**, 3149–3152 (2000).
- Sun, J. Z. Spin-current interaction with a monodomain magnetic body: a model study. *Phys. Rev. B* **62**, 570–578 (2000).
- Grollier, J. et al. Field dependence of magnetization reversal by spin transfer. *Phys. Rev. B* **67**, 174402 (2003).
- Özyilmaz, B. et al. Current-induced magnetization reversal in high magnetic fields in Co/Cu/Co Nanopillars. *Phys. Rev. Lett.* **91**, 067203 (2003).
- Manchon, A. et al. Current-induced spin-orbit torques in ferromagnetic and antiferromagnetic systems. *Rev. Mod. Phys.* **91**, 035004 (2019).
- Sinova, J., Valenzuela, S. O., Wunderlich, J., Back, C. H. & Jungwirth, T. Spin Hall effects. *Rev. Mod. Phys.* **87**, 1213–1260 (2015).
- Shao, Q. et al. Roadmap of spin-orbit torques. *IEEE Trans. Magn.* **57**, 1–39 (2021).
- Tsoi, M. et al. Excitation of a magnetic multilayer by an electric current. *Phys. Rev. Lett.* **80**, 4281–4284 (1998).
- Kiselev, S. I. et al. Microwave oscillations of a nanomagnet driven by a spin-polarized current. *Nature* **425**, 380–383 (2003).
- Demidov, V. E. et al. Magnetic nano-oscillator driven by pure spin current. *Nat. Mater.* **11**, 1028–1031 (2012).
- Chen, T. et al. Spin-torque and spin-hall nano-oscillators. *Proc. IEEE* **104**, 1919–1945 (2016).
- Mazraati, H. et al. Auto-oscillating spin-wave modes of constriction-based spin hall nano-oscillators in weak in-plane fields. *Phys. Rev. Appl.* **10**, 054017 (2018).
- Ahlberg, M., Jiang, S., Khymyn, R., Chung, S. & Åkerman, J. *Magnetic Droplet Solitons* (eds Bandyopadhyay S. and Barman, A.) 183–216 (Springer, 2024).
- Borders, W. A. et al. Integer factorization using stochastic magnetic tunnel junctions. *Nature* **573**, 390–393 (2019).
- Makiuchi, T. et al. Parametron on magnetic dot: stable and stochastic operation. *Appl. Phys. Lett.* **118**, 022402 (2021).
- Meng, H., Lum, W. H., Sbiaa, R., Lua, S. Y. H. & Tan, H. K. Annealing effects on CoFeB–MgO magnetic tunnel junctions with perpendicular anisotropy. *J. Appl. Phys.* **110**, 033904 (2011).
- Aleksandrov, Y. et al. Evolution of the interfacial magnetic anisotropy in MgO/CoFeB/Ta/Ru based multilayers as a function of annealing temperature. *AIP Adv.* **6**, 065321 (2016).
- Liu, L., Moriyama, T., Ralph, D. C. & Buhrman, R. A. Spin-torque ferromagnetic resonance induced by the spin hall effect. *Phys. Rev. Lett.* **106**, 036601 (2011).
- Lee, K.-S., Lee, S.-W., Min, B.-C. & Lee, K.-J. Threshold current for switching of a perpendicular magnetic layer induced by spin Hall effect. *Appl. Phys. Lett.* **102**, 112410 (2013).
- Nakayama, H. et al. Spin Hall magnetoresistance induced by a nonequilibrium proximity effect. *Phys. Rev. Lett.* **110**, 206601 (2013).

48. Chen, Y.-T. et al. Theory of spin Hall magnetoresistance. *Phys. Rev. B* **87**, 144411 (2013).
49. Tulapurkar, A. A. et al. Spin-torque diode effect in magnetic tunnel junctions. *Nature* **438**, 339–342 (2005).
50. Fang, D. et al. Spin-orbit-driven ferromagnetic resonance. *Nat. Nanotechnol.* **6**, 413–417 (2011).
51. Ando, K. et al. Electric manipulation of spin relaxation using the spin Hall effect. *Phys. Rev. Lett.* **101**, 036601 (2008).
52. Duan, Z. et al. Nanowire spin torque oscillator driven by spin orbit torques. *Nat. Commun.* **5**, 5616 (2014).
53. Kim, J.-S. et al. Control of crystallization and magnetic properties of cofeb by boron concentration. *Sci. Rep.* **12**, 4549 (2022).
54. Pai, C.-F. et al. Spin transfer torque devices utilizing the giant spin Hall effect of tungsten. *Appl. Phys. Lett.* **101**, 122404 (2012).
55. Avci, C. O., Mendil, J., Beach, G. S. D. & Gambardella, P. Origins of the unidirectional spin hall magnetoresistance in metallic bilayers. *Phys. Rev. Lett.* **121**, 087207 (2018).
56. Borisenko, I. V., Demidov, V. E., Urazhdin, S., Rinkevich, A. B. & Demokritov, S. O. Relation between unidirectional spin hall magnetoresistance and spin current-driven magnon generation. *Appl. Phys. Lett.* **113**, 062403 (2018).
57. Xiao, J., Bauer, G. E. W., Uchida, K. -c, Saitoh, E. & Maekawa, S. Theory of magnon-driven spin seebeck effect. *Phys. Rev. B* **81**, 214418 (2010).
58. Teschl, G. *Ordinary Differential Equations and Dynamical Systems* Vol. 140 (American Mathematical Society, 2012).
59. Newhall, K. A. & Vanden-Eijnden, E. Averaged equation for energy diffusion on a graph reveals bifurcation diagram and thermally assisted reversal times in spin-torque driven nanomagnets. *J. Appl. Phys.* **113**, 184105 (2013).
60. Taniguchi, T., Utsumi, Y. & Imamura, H. Thermally activated switching rate of a nanomagnet in the presence of spin torque. *Phys. Rev. B* **88**, 214414 (2013).
61. Harms, J. S., Yuan, H. Y. & Duine, R. A. Antimagnonics. *AIP Adv.* **14**, 025303 (2024).
62. Salakhutdinov, R., Mnih, A. & Hinton, G. Restricted boltzmann machines for collaborative filtering. In *Proc. 24th International Conference on Machine Learning* (ed. Ghahramani, Z.) 791–798 (2007).
63. Bereux, N., Decelle, A., Furtlehner, C., Rosset, L. & Seoane, B. Fast training and sampling of Restricted Boltzmann Machines. In *13th International Conference on Learning Representations 2025* (ICLR, 2025).
64. Chen, H. & Murray, A. A continuous restricted boltzmann machine with a hardware- amenable learning algorithm. In *Artificial Neural Networks—ICANN 2002* (ed. Dorronsoro, J. R.) 358–363 (Springer, 2002).
65. Chen, H. & Murray, A. Continuous restricted boltzmann machine with an implementable training algorithm. *IEE Proc. Vis. Image Signal Process.* **150**, 153–158 (2003).
66. Borders, W. A., Pervaiz, A. Z., Fukami, S. et al. Integer factorization using stochastic magnetic tunnel junctions. *Nature* **573**, 390–393 (2019).
67. Kruglyak, V., Demokritov, S. & Grundler, D. Magnonics. *J. Phys. D* **43**, 260301 (2010).
68. Chumak, A. V., Vasyuchka, V. I., Serga, A. A. & Hillebrands, B. Magnon spintronics. *Nat. Phys.* **11**, 453–461 (2015).
69. Barman, A. et al. The 2021 magnonics roadmap. *J. Phys. Condens. Matter* **33**, 413001 (2021).
70. Chowdhury, S. et al. A full-stack view of probabilistic computing with p-bits: devices, architectures, and algorithms. *IEEE J. Explor. Solid-State Comput. Devices Circuits* **9**, 1–11 (2023).
71. Karadza, E. et al. Dynamical stabilization of inverted magnetization and antimagnons by spin injection in an extended magnetic system. <https://doi.org/10.48550/arXiv.2601.09569> (2026).

Publisher's note Springer Nature remains neutral with regard to jurisdictional claims in published maps and institutional affiliations.

Open Access This article is licensed under a Creative Commons Attribution 4.0 International License, which permits use, sharing, adaptation, distribution and reproduction in any medium or format, as long as you give appropriate credit to the original author(s) and the source, provide a link to the Creative Commons licence, and indicate if changes were made. The images or other third party material in this article are included in the article's Creative Commons licence, unless indicated otherwise in a credit line to the material. If material is not included in the article's Creative Commons licence and your intended use is not permitted by statutory regulation or exceeds the permitted use, you will need to obtain permission directly from the copyright holder. To view a copy of this licence, visit <http://creativecommons.org/licenses/by/4.0/>.

© The Author(s) 2026

Methods

Definition of β

We parametrize the efficiency of current-induced STTs in the planar SOT geometry by the fit parameter $\beta = \hbar\theta_{\text{SH}}/(2e\mu_0M_s w d_m d_w)$, where \hbar , e , w , d_m and d_w are the reduced Planck constant, the elementary charge, the device bar width and the thicknesses of CoFeB and W layers, respectively.

Thin film preparation, post-annealing and device fabrication

Thin films were grown on thermally oxidized Si (Si–O/Si) substrates by magnetron sputtering in an ultrahigh vacuum apparatus with the base pressure below 2×10^{-7} Pa. The stacking of the thin films was Si substrate|Si–O|W (3 nm)|CoFeB (2 nm)|MgO (3 nm). All layers were deposited at ambient temperature under the Ar gas pressure of ~ 5 mTorr. The W and CoFeB (atomic composition of $\text{Co}_{20}\text{Fe}_{60}\text{B}_{20}$) targets were sputtered using dc power supplies, whereas the MgO target was sputtered using a radio frequency power supply. The deposition rates were set to 0.029 nm s^{-1} for W, 0.022 nm s^{-1} for CoFeB and 0.0016 nm s^{-1} for MgO. The structural characterization of one of the post-annealed W|CoFeB|MgO samples was carried out by scanning transmission electron microscopy and shown in Supplementary Note 2. After each sputter-deposition, the films were transferred to the vacuum furnace with the base pressure below 1×10^{-4} Pa in which the films were annealed at a target temperature for 1 h—see Supplementary Note 1 for the annealing condition. The thin films were patterned into a rectangle with $10 \mu\text{m}$ width and $40 \mu\text{m}$ length by Ar ion milling using standard optical lithography, onto which Au electrodes patterned into a coplanar waveguide were made by sputtering and lift-off techniques.

ST-FMR and MR measurements

The devices were measured in a microwave prober system to minimize the losses between a microwave signal generator and the device. Typically, we inject microwaves with a power of 13 dBm by the signal generator, with amplitudes modulated by 25% at a frequency of 10 kHz. For ST-FMR measurements, this $I_{\text{mw}} \sin(2\pi ft)$ induces a rectification voltage across the device that is measured through a bias tee using a lock-in amplifier set to 10 kHz. I_{dc} is applied through the bias tee and a 10 k Ω resistor. The measured data of V are fitted using the following functions:

$$V = V_0 + V_{\text{sym}} \frac{\Delta H^2}{(H_{\text{ext}} - H_{\text{res}})^2 + \Delta H^2} + V_{\text{asy}} \frac{\Delta H(H_{\text{ext}} - H_{\text{res}})}{(H_{\text{ext}} - H_{\text{res}})^2 + \Delta H^2},$$

where V_0 , V_{sym} and V_{asy} are the field-independent voltage, the amplitude of the symmetric and antisymmetric components around H_{res} . We extract H_{res} for Fig. 4c by using H_{ext} that maximized and minimized the peak amplitude. We measured MR by applying I_{dc} through the 10 k Ω resistor in series.

Macrospin simulations

The LLG equation with a damping-like spin-torque term reads

$$\frac{d\mathbf{n}}{dt} = -\frac{\gamma}{1+\alpha^2} \mathbf{n} \times \mathbf{B}^{\text{eff}} - \frac{\gamma\alpha}{1+\alpha^2} \mathbf{n} \times (\mathbf{n} \times \mathbf{B}^{\text{eff}}) - \gamma\beta I_{\text{dc}} \mathbf{n} \times (\mathbf{n} \times \boldsymbol{\sigma}), \quad (4)$$

where \mathbf{n} is the dimensionless unit vector of the magnetization, \mathbf{B}^{eff} is the effective field in tesla, $\alpha = 0.09$ is the dimensionless Gilbert damping, $\gamma = 1.76 \times 10^{11} \text{ rad s}^{-1} \text{ T}^{-1}$ is the gyromagnetic ratio and $\boldsymbol{\sigma}$ is the direction of the electron spin polarization. The STT has a strength βj with $\beta = \hbar\theta_{\text{SH}}/(2e\mu_0M_s w d_m d_w) = 2.6 \times 10^6$ where $\theta_{\text{SH}} = 0.22$ is the spin-Hall angle, $M_s = 758 \text{ kA m}^{-1}$ is the saturation magnetization of CoFeB, $w = 10 \mu\text{m}$ is the width of the sample (perpendicular to the current direction) and $d_w = 3 \text{ nm}$ is the thickness of the normal metal, and we assume all of the electronic current flows through this layer due to the higher conductivity. $d_m = 1 \text{ nm}$ is the thickness of the magnetic layer. We integrate the equation of motion numerically using a fourth-order Runge-Kutta scheme with a time-step $\Delta t = 0.01 \text{ ps}$. The effective field contains terms for the applied field, the demagnetizing effect of a thin film and a PMA that is

$$\mathbf{B}^{\text{eff}} = \mu_0 \mathbf{H}_{\text{ext}} - \left(\mu_0 M_s - \frac{2K_{\perp}}{M_s} \right) \mathbf{e}_z + \boldsymbol{\xi}, \quad (5)$$

where μ_0 is the vacuum permeability, $\mu_0 \mathbf{H}_{\text{ext}}$ is the externally applied magnetic field in tesla, $K_{\perp} = 327 \text{ kJ m}^{-3}$ is the magneto-crystalline anisotropy energy density and \mathbf{e}_z is a unit vector along the z -direction. $\boldsymbol{\xi}$ is a stochastic thermal field in tesla with white noise characteristics governed by the fluctuation–dissipation theorem $\langle \boldsymbol{\xi} \rangle = 0$; $\langle \xi(t)\xi(t') \rangle = \delta(t-t')(2\alpha k_B T)/(\gamma(1+\alpha^2)M_s V_a)$, where $V_a = 1 \times 25 \times 25 \text{ nm}^3$ is the effective volume of a macrospin region in the extended film. We include the effect of Joule heating by renormalizing the anisotropy and magnetization at a given temperature. See Supplementary Note 8 for more details.

Data availability

The data presented in the Article and its Supplementary Information are available from the corresponding authors upon reasonable request.

Code availability

The code utilized in the Article and its Supplementary Information are available from the corresponding authors upon reasonable request.

Acknowledgements

We thank P. Pirro, A. Koujok, M. Kläui, O. Klein, C. Back, L. Chen, E. Saitoh, K. Çamsarı and T. Taniguchi for stimulating discussions. H.K. thanks the Leverhulme Trust for financial support via their research fellowship (grant no. RF-2024-317) and the Engineering and Physical Sciences Research Council (EPSRC) for support via grant no. EP/X015661/1. J.B. acknowledges funding from a Royal Society University Research Fellowship. H.Y. thanks the EPSRC for funding through the EPSRC DTP studentship (grant nos. EP/T517793/1 and EP/W524335/1). D.P. is supported by the EPSRC and SFI Centre for Doctoral Training in Advanced Characterisation of Materials (grant reference no. EP/S023259/1). This project was supported by JSPS KAKENHI (grant nos. 21K13886, 24K00576, JP23H00232, 22H04965, JP24H02231, JP25K17931 and 25H00837), X-NICS of MEXT (grant no. JPJ011438) and JST PRESTO (grant no. JPMJPR20LB). Part of this work was undertaken on the Aire HPC system at the University of Leeds, UK. The device fabrication was partly carried out at the Cooperative Research and Development Center for Advanced Materials, Institute for Materials Research, Tohoku University. The authors thank T. Sasaki for their Au film deposition. This work was partially supported by the Collaborative Research Center on Energy Materials, Institute for Materials Research (E-IMR), Tohoku University. H.K. and T.S. acknowledge support by the GIMRT Program of the Institute for Materials Research and by the Invitational Fellowship Program for Collaborative Research with International Researcher 2024, Tohoku University. J.B. and K.Y. acknowledge support from a Royal Society International Exchange 2023 Cost Share (JSPS)/JSPS Bilateral Program number JPJSBP120245708. K.S. is supported by the Eric and Wendy Schmidt AI in Science Postdoctoral Fellowship, a Schmidt Sciences program and the Imperial College Research Fellowship.

Author contributions

H.K., T.S. and K.Y. started this study in summer 2022, supported by the visiting professorship programme at Institute for Materials Research, Tohoku University. H.K., T.S. and V.K.K. grew thin films and fabricated them into micro-devices. H.K., T.S., T.Y., T.D., D.P. and K.D.S. performed magnetic and transport measurements presented in this work. H.K., T.S., T.D., D.P. and K.Y. carried out data analysis, supported by all the coauthors. K.Y. theorized the dynamical stability analysis. K.Y. and G.E.W.B. provided critical insights for the early state of this study. J.B. performed the macrospin simulations and contributed to finalize this study. H.Y. performed the continuous RBM work supervised by H.K. T.Y. and X.H. performed the structural analysis

by STEM. H.K., K.Y., J.B., G.E.W.B. and T.S. prepared the manuscript where the rest provided comments.

Competing interests

The authors declare no competing interests.

Additional information

Supplementary information The online version contains supplementary material available at <https://doi.org/10.1038/s41563-026-02510-z>.

Correspondence and requests for materials should be addressed to Hidekazu Kurebayashi, Kei Yamamoto or Takeshi Seki.

Peer review information *Nature Materials* thanks Andrew Kent, Kyung-Jin Lee and the other, anonymous, reviewer(s) for their contribution to the peer review of this work.

Reprints and permissions information is available at www.nature.com/reprints.